

Modeling interfaces between solids: Application to Li battery materials

N. D. Lepley and N. A. W. Holzwarth*

Department of Physics, Wake Forest University, Winston-Salem, North Carolina 27109-7507, USA

(Received 31 August 2015; revised manuscript received 10 November 2015; published 1 December 2015)

We present a general scheme to model an energy for analyzing interfaces between crystalline solids, quantitatively including the effects of varying configurations and lattice strain. This scheme is successfully applied to the modeling of likely interface geometries of several solid state battery materials including Li metal, Li_3PO_4 , Li_3PS_4 , Li_2O , and Li_2S . Our formalism, together with a partial density of states analysis, allows us to characterize the thickness, stability, and transport properties of these interfaces. We find that all of the interfaces in this study are stable with the exception of $\text{Li}_3\text{PS}_4/\text{Li}$. For this chemically unstable interface, the partial density of states helps to identify mechanisms associated with the interface reactions. Our energetic measure of interfaces and our analysis of the band alignment between interface materials indicate multiple factors, which may be predictors of interface stability, an important property of solid electrolyte systems.

DOI: [10.1103/PhysRevB.92.214201](https://doi.org/10.1103/PhysRevB.92.214201)

PACS number(s): 68.35.Md, 82.45.Gj, 82.47.Aa

I. INTRODUCTION**A. Overview**

The study of the detailed geometries and energetics of interfaces between solids, important to a number of technologies, provides interesting challenges to condensed matter modeling. These challenges include the large number of possible interface configurations, the role of lattice strains and defects, and, in some cases, the occurrence of chemical reactions. There have been a number of review monographs and articles that have described many of these effects [1–3] as have a number of detailed case studies [4–8]. In the present work, we highlight and extend the methods needed to model these effects and use them to investigate interfaces relevant to the development of solid state batteries.

There is growing evidence that solid state battery electrolytes offer stability and efficiency advantages, especially wider electrochemical windows, relative to liquid electrolyte chemistries [9]. Interface properties play an important role in solid state battery performance and well-characterized electrolyte interfaces have been the focus of recent experimental [10] and theoretical [11,12] work. The study of interfaces also provides a mechanism for directly probing the electrochemical window of potential solid electrolyte materials. As a result, there is a compelling incentive to study and to optimize interfaces between solid electrolytes and anode materials, between solid electrolytes and cathode materials, and between solid electrolytes and buffer layer materials. Computer simulation applied to specific idealized examples of these interfaces can advance this effort in terms of analyzing likely interface geometries and their energies.

The interface systems considered in this study follow our previous studies of lithium phosphate and thiophosphate interfaces [13], including the $\text{Li}_3\text{PO}_4/\text{Li}$, $\text{Li}_3\text{PS}_4/\text{Li}$, and $\text{Li}_3\text{PS}_4/\text{Li}_2\text{S}$ interfaces. Our previous work suggests that Li_2S can serve as a buffer layer for lithium thiophosphate electrolytes, which motivated an examination of $\text{Li}_2\text{S}/\text{Li}$ interfaces in this study. In addition, we also consider $\text{Li}_2\text{O}/\text{Li}$ interfaces which have been studied by a number of authors

[14–22]. While these interfaces are predominantly related to possible electrolyte/anode materials in Li ion batteries [23], our methodology should apply equally well to solid state cathode interfaces [11,24].

The manuscript is organized as follows. Section IB introduces some of the general concepts of interface analysis. Section IIA presents the general equations used in this work, while Sec. IIB, presents the calculational details. Results for equilibrium interface energies are detailed in Sec. IIIA, with a summarizing table presented at the end of the section. Analysis of the partial densities of states of the interface systems is presented in Sec. IIIB. In addition to the study of the equilibrium systems, some aspects of ion transport and interface reactions are presented in Sec. IIIC. The results are discussed in Sec. IV and concluding remarks are contained in Sec. V.

B. Interfaces between solid materials

For a given interface, its configuration Ω can be described in terms of the positions of all of the atoms that make up the interface. Among the innumerable possibilities for the interface configuration Ω between materials a and b , there are three broad classifications based on the extent to which the lattices of the two materials align [1,3]. A coherent interface exhibits nearly perfect compatibility between the lattice constants of the two materials at the interface, and the lattice planes are continuous across the interface. The resulting interface structure can be described by a single periodic phase, with periodicity set by the lattice constants of the composite system. At a semicoherent interface, the two materials have similar but not equal lattice spacing, which results in lattice strain at the interface. In order to relieve this strain, semicoherent interfaces typically involve defect sites at the interface, so that not all of the lattice planes are continuous across the interface boundary. For an incoherent interface, there is significant mismatch between the lattice constants of the two materials, and there is no significant continuity of lattice planes across the interface.

A number of energetic measures to characterize interfaces have been defined in the literature [1–8]. The interface energy (γ_{ab}) between materials a and b is defined as the energy

*natalie@wfu.edu

difference between an interface system and the bulk energy of the two materials that comprise it for a given Ω :

$$\gamma_{ab}(\Omega) = \frac{E_{ab}(\Omega, A, n_a, n_b) - n_a E_a - n_b E_b}{A}. \quad (1)$$

Here, E_{ab} denotes the total energy of the complete system containing the interface, and it depends on how many formula units of materials a and b comprise the interface (n_a and n_b , respectively), as well as on the configuration Ω and the interfacial area A . E_a and E_b denote the bulk energy per formula unit for materials a and b , respectively. Versions of Eq. (1) appropriate for nonstoichiometric interfaces, as well as systems at varying temperatures and pressures exist in the literature [1,3], but are not covered in detail here.

Another energy measure is the ideal work W_{ab} of adhesion or separation [2,5], which models the idealized separation of the interface into two surfaces in vacuum:¹

$$W_{ab}(\Omega) = \gamma_{a,\text{vac}}(\Omega) + \gamma_{b,\text{vac}}(\Omega) - \gamma_{ab}(\Omega). \quad (2)$$

In this expression, $\gamma_{a,\text{vac}}(\Omega)$ and $\gamma_{b,\text{vac}}(\Omega)$ denote the ideal surface energies of materials a and b in vacuum for the particular cleavages implied by the configuration Ω .

Ω depends on the positions of all of the atoms at the interface and includes not only the detailed geometries, but also the effects of cleavage planes, interface alignment, and defect structures produced by lattice mismatch. There are, in principle, many possible interface configurations, but in practice we expect likely interfaces to exhibit both relatively low interface energies and local order approximately consistent with either the bulk ordering of material a or with that of material b , or with both. While there may not be a single value of γ_{ab} for two materials, by sampling likely configurations Ω we can establish both a likely value for γ_{ab} and an estimate for the range of its variation.

Because γ_{ab} is an intensive energy, it can in principle be computed by determining the γ_{ab} values of successively larger subregions of the interface using the convergence of the limit

$$\lim_{\Omega_s \rightarrow \Omega} [\gamma_{ab}(\Omega_s)] = \gamma_{ab}(\Omega), \quad (3)$$

where Ω_s denotes the atomic configuration in some sample interface volume. Because Ω may exhibit periodic structure on a variety of different length scales [1], $\lim_{\Omega_s \rightarrow \Omega} [\gamma_{ab}(\Omega_s)]$ is not monotonic and correctly computing this limit requires careful consideration of possible interface structures, especially dislocation defects caused by lattice mismatch between the two interface materials.

In the following sections, we further develop these ideas to provide a practical scheme for the simulation of interface systems. While our formulation focuses primarily on relatively ordered interfaces, by explicitly accounting for the lattice strain energy, we are able to estimate the likely extent of interface disorder.

¹Reference [2] distinguishes the work of separation and adhesion, such that the final state of the former is an ideal stoichiometric surface, while the final state of the latter includes effects of diffusion and distortion.

II. FORMALISM AND METHODS

A. Formalism

While the definition of the interface energy given in Eq. (1) is fully general, it is prohibitively expensive to evaluate the energy of realistic trial configurations Ω and difficult even to satisfactorily converge the sampling limit Ω_s . In the interest of efficiency, instead we consider approximate interface configurations $\tilde{\Omega}$ that correspond to periodic ordered phases we label $\tilde{\Omega}$. In the case of a coherent interface, where there is no mismatch between the lattices of the interface materials the interface phase described by Ω is automatically periodic and $\tilde{\Omega} = \Omega$.

The more likely case is that of the semicoherent interface, where there is some degree of lattice mismatch between the two phases. By imposing periodic boundary conditions to the simulation system, a lattice strain is necessarily introduced into the system to bring the two lattices into alignment. This strain energy scales with the amount of material under strain and can be assumed to have the functional form $\tilde{E}_{\text{str}}(\tilde{\Omega}, n_a, n_b)$. Consequently, while we can still define an interface energy according to Eq. (1), it is no longer an intensive quantity; the interface energy calculated in the periodic cell now depends on n_a and n_b :

$$\tilde{\gamma}_{ab}(\tilde{\Omega}, n_a, n_b) = \frac{\tilde{E}_{ab}(\tilde{\Omega}, A, n_a, n_b) - n_a E_a - n_b E_b}{A}. \quad (4)$$

The terms of this equation are defined identically to those in Eq. (1), although for clarity we label the quantities computed in our periodic cell with a tilde. Because of the periodic boundary conditions, each simulation cell contains two interfaces and the area A represents the combined area of both. Correspondingly, $\tilde{\gamma}_{ab}(\tilde{\Omega}, n_a, n_b)$ is the average of the two interface energies. Because of the lattice strain, $\tilde{\gamma}_{ab}$ does not converge with respect to system size in the direction perpendicular to the interface. For the true interface configuration Ω , the strain is relieved by the formation of dislocation defects so the strain energy $\tilde{E}_{\text{str}}(\tilde{\Omega}, n_a, n_b)$ present in $\tilde{\gamma}_{ab}$ is unphysically large.

Subtracting the strain energy from $\tilde{\gamma}_{ab}$ is equivalent to calculating the interface energy in the coherent limit, and is given by the equation

$$\begin{aligned} \tilde{\gamma}_{ab}^{\text{lim}}(\tilde{\Omega}) &= \tilde{\gamma}_{ab}(\tilde{\Omega}, n_a, n_b) - \frac{\tilde{E}_{\text{str}}(\tilde{\Omega}, n_a, n_b)}{A} \\ &= \frac{\tilde{E}_{ab}(\tilde{\Omega}, A, n_a, n_b) - n_a E_a - n_b E_b - \tilde{E}_{\text{str}}(\tilde{\Omega}, n_a, n_b)}{A}. \end{aligned} \quad (5)$$

In this equation, \tilde{E}_{str} denotes the strain energy, A is the area of the interface, $\tilde{\Omega}$ the interface configuration in the periodic cell, n_a and n_b represent the number of formula units of materials a and b , and E_a and E_b represent the energy per formula unit of the two materials in their unstrained bulk configurations. Unlike $\tilde{\gamma}_{ab}(\tilde{\Omega}, n_a, n_b)$, $\tilde{\gamma}_{ab}^{\text{lim}}(\tilde{\Omega})$ does not depend on n_a or n_b , and thus converges much better with respect to system size and provides a better estimate of $\gamma_{ab}(\Omega)$. Similar ideas were previously discussed by Benedek *et al.* [3].

The definition of $\tilde{\gamma}_{ab}^{\text{lim}}(\tilde{\Omega})$ assumes that the interface interaction has a finite range and that beyond some threshold value of n_a or n_b additional formula units of material a or b only affect

the strain energy. \tilde{E}_{str} can be determined in multiple ways, but the approach taken in this work exploits the dependence of both $\tilde{\gamma}_{ab}$ and \tilde{E}_{str} on the system size. We calculated $\tilde{\gamma}_{ab}$ for several interface systems which had the same interface configuration $\tilde{\Omega}$ and had their lattices fixed to the bulk values of material a , but which had different amounts of material b . For these systems beyond the threshold value of n_b Eq. (5) can be rearranged to obtain the relation

$$\tilde{\gamma}_{ab}(\tilde{\Omega}, n_b) = \tilde{\gamma}_{ab}^{\text{lim}}(\tilde{\Omega}) + n_b \sigma, \quad (6)$$

where σ is a constant related to the strain energy in material b . This approach both enables an explicit treatment of the strain energy and makes the results less sensitive to possible phase changes in material b due to the combined effects of the interface and interface strain. Plotting $\tilde{\gamma}_{ab}(\tilde{\Omega}, n_b)$ against n_b yields a straight line with slope σ and intercept $\tilde{\gamma}_{ab}^{\text{lim}}(\tilde{\Omega})$. As an aside, we note that instead of the explicit inclusion of a strain energy term as in Eq. (5), some authors account for strain by replacing the E_a and E_b terms in Eq. (4) with the per formula unit energies of the strained bulk systems \tilde{E}_a and \tilde{E}_b [4,5].

It is important to note that in subtracting the strain energy from $\tilde{\gamma}_{ab}(\tilde{\Omega})$ to obtain $\tilde{\gamma}_{ab}^{\text{lim}}(\tilde{\Omega})$, we do not capture the energy contributions from the defects that relieve the strain in the real system. $\tilde{\gamma}_{ab}^{\text{lim}}(\tilde{\Omega})$ is thus an underestimate of the true interface energy $\gamma_{ab}(\Omega)$, which should fall between $\tilde{\gamma}_{ab}^{\text{lim}}$ and $\tilde{\gamma}_{ab}$. For coherent and semicoherent cases where $\tilde{\Omega} \approx \Omega$, this gives the relation

$$\tilde{\gamma}_{ab}^{\text{lim}}(\tilde{\Omega}) \leq \gamma_{ab}(\Omega) \leq \tilde{\gamma}_{ab}(\tilde{\Omega}, n_a, n_b) \quad (7)$$

with the equalities corresponding to the coherent case. The difference between $\tilde{\gamma}_{ab}$ and $\tilde{\gamma}_{ab}^{\text{lim}}$ can thus provide an error bound for the difference between the true interface energy and the energy calculated in the coherent limit. This error bound provides an estimate of the error associated with the limited in-plane size of the periodic supercell approximation of the interface, i.e., the in-plane lattice supercell error.

B. Methods

1. General computational methods

The computational methods are based on density functional theory (DFT) [25,26] using the projector augmented wave (PAW) formalism [27] as implemented in the QUANTUM ESPRESSO software package [28]. The PAW basis and projector functions needed for each atom were generated by the ATOMPAW code [29]. The exchange-correlation functional used in this work was the local density approximation (LDA) [30], which has been used in previous studies [13] and has been shown to work well for this class of materials. The Bloch wave functions were well-converged within a plane wave cutoff of 64 Ry. The k -space sampling was evaluated using a Monkhorst Pack scheme [31] with a typical grid volume of 0.03 \AA^{-3} or smaller and Gaussian smearing of 0.001 Ry. The partial densities of states were determined from weight factors for each state approximating the electron density within the augmentation sphere about each atomic site as explained in Ref. [13] and then averaged over atomic sites within a given set s . Explicitly, the partial density of states for a set of atomic

sites s is given by

$$N^s(E) = \frac{1}{M_s} \sum_{a \in s} N^a(E), \quad \text{where}$$

$$N^a(E) = \left(\sum_{nk} W_{\mathbf{k}} Q_{nk}^a \delta(E - E_{nk}) \right) \text{ and} \quad (8)$$

where the M_s denotes the number of atoms a in set s and $W_{\mathbf{k}}$ denotes the Brillouin zone weighting factor for approximating the Brillouin zone integration. Here the factor Q_{nk}^a is given by the charge within the augmentation sphere of atom a for state $n\mathbf{k}$. In practice, the δ function is represented by a Gaussian smoothing function with a width of 0.14 eV. The k point sampling for evaluating the partial densities of states was typically eight times denser than that used for the structural optimization studies and in some cases was further increased in order to generate smoother curves. The ‘‘nudged elastic band’’ (NEB) method [32–34], as programed in the QUANTUM ESPRESSO package was used to estimate activation energies. Visualizations of the supercell configurations were constructed using the XCRYSDEN [35,36] and VESTA [37] software packages.

2. Interface representations

Supercells constructed with alternating sections of material a and material b were used to evaluate Eqs. (4) and (6). For the interfaces considered in this study, we chose the electrolytes as material a , which means that the supercell lattice constants were fixed in accordance with Eq. (6) to their calculated bulk values which are listed in Table I. The slab geometry and periodic boundary conditions resulted in the formation of two a - b interfaces in each simulation cell, and for most systems the interfaces were constructed to be symmetrically equivalent.

In order to observe the linear relationship implied by Eq. (6), we constructed sets of supercells with a fixed interface configuration $\tilde{\Omega}$ and a varying number of layers of material b . Possible interface configurations were discovered by optimizing both the atomic positions and the supercell lattice constant normal to the interface of trial structures. Because the number of possible configurations is large and because the relaxation algorithm only discovers local minima, we started the optimization from several globally distinct initial configurations to better sample the configuration space. These initial configurations were generated in several ways over course of this study.

TABLE I. Lattice parameters (in \AA) and heats of formation [13] (ΔH in eV per formula unit) calculated for bulk materials in this study.

Material	Phase	Lattice Constants	ΔH
Li	$Im\bar{3}m$	3.36	0.00
Li	$Fm\bar{3}m$	4.23	0.00
Li ₂ O	$Fm\bar{3}m$	4.53	− 6.10
Li ₂ S	$Fm\bar{3}m$	5.57	− 4.30
β -Li ₃ PO ₄	$Pmn2_1$	6.00, 5.13, 4.74	− 21.23
γ -Li ₃ PO ₄	$Pnma$	10.28, 5.99, 4.82	− 21.20
γ -Li ₃ PS ₄	$Pmn2_1$	7.55, 6.45, 6.05	− 8.37

One approach common in the literature is to choose surface planes for materials a and b with similar lattice constants in order to construct a supercell with minimal lattice mismatch at the interface. While we followed this approach for many of our interface systems, of the reported configurations, only the $\text{Li}_3\text{PS}_4/\text{Li}_2\text{S}$ interface configuration was determined using this method alone.

One limitation of this approach is that the high degree of order in the initial configuration limits the ability of the optimization algorithm to find interface structures that differ significantly from the initial guess. Determining likely trial structures for a Li metal in particular is complicated by the existence at low temperature of several bulk phases with very similar energies [38,39]. As a consequence, a naively constructed sequence of Li structures can not only fail to adequately sample the configuration space, but also result in Li metal slabs that contain defects and heterogeneous phases.

In one attempt to address this difficulty, we constructed initial Li configurations using orthorhombic grids with a structure based on that of Li monolayers. The relaxation algorithm tended to preserve the symmetry of the grid and the resulting configurations $\tilde{\Omega}$ exhibited relatively large strain parameters σ . We also generated initial configurations by adding random noise to the positions of atoms in ordered Li structures before optimizing the interface. Applying this method to a relatively small number of Li atoms, generally resulted in an ordered Li structure, which was less sensitive to the initial guess and which could be systematically extended along the interface normal direction to generate slabs of varying thicknesses. While this method is particularly useful for Li, we expect it to also be applicable to other simple materials.

The results presented below all follow the approach described by Eq. (6) based on a series of three or more consistent supercell simulations. These results were corroborated by additional simulations using larger supercells and additional configurations.

III. RESULTS

A. Interface configurations and their energies

The lattice constants for the bulk materials used in this study are listed in Table I. Note that due to our use of the LDA exchange-correlation functional there is a systematic (2%) underestimate of the lattice constants. However, it has been well-documented [13,40] that the relative coordinates and the energetics are well-represented in the class of materials considered here. Using the formalism developed in the previous section, we simulated solid-solid interfaces for several electrolyte materials. The individual case studies are presented here, and the interface energies $\tilde{\gamma}_{ab}^{\text{lim}}$ for the various materials and interface configurations are summarized in Table II. Whenever possible, the interface supercells were constructed symmetrically so that the reported value of $\tilde{\gamma}_{ab}^{\text{lim}}$ characterizes both interfaces in each supercell.

1. $\text{Li}_2\text{O}/\text{Li}$

The interface between Li_2O and Li metal has been well-characterized in the literature [14–22]. In this work, we

TABLE II. Summary of the calculated values of $\tilde{\gamma}_{ab}^{\text{lim}}$ in $\text{meV}/\text{\AA}^2$ (N.B. $1 \text{ meV}/\text{\AA}^2 = 16.02 \text{ mJ}/\text{m}^2$). Also included are the calculated strain energies σ expressed in units of $\text{meV}/\text{\AA}^2/\text{formula unit}$ of material b . The final column lists the corresponding structural diagrams.

Configuration ($\tilde{\Omega}$)	$\tilde{\gamma}_{ab}^{\text{lim}}$ ($\text{meV}/\text{\AA}^2$)	σ ($\text{meV}/\text{\AA}^2/\text{FU}$)	Visualization
$\text{Li}_2\text{O}[100]/\text{vac}$	304	–	–
$\text{Li}_2\text{O}[110]/\text{vac}$	72	–	–
$\text{Li}_2\text{O}[110]/\text{Li}(\tilde{\Omega}_1)$	30	6.1	Fig. 1(a)
$\text{Li}_2\text{O}[110]/\text{Li}(\tilde{\Omega}_2)$	26	0.2	Fig. 1(b)
$\text{Li}_2\text{S}[100]/\text{vac}$	162	–	–
$\text{Li}_2\text{S}[110]/\text{vac}$	41	–	–
$\text{Li}_2\text{S}[110]/\text{Li}(\tilde{\Omega}_1)$	47	4.0	Fig. 3(a)
$\text{Li}_2\text{S}[110]/\text{Li}(\tilde{\Omega}_2)$	11	4.0	Fig. 3(b)
$\text{Li}_2\text{S}[110]/\text{Li}(\tilde{\Omega}_3)$	19	0.2	Fig. 3(c)
$\text{Li}_2\text{S}[100]/\text{Li}(\tilde{\Omega}_4)$	19	0.0	Fig. 3(d)
$\beta\text{-Li}_3\text{PO}_4[010]/\text{vac}$	39	–	–
$\gamma\text{-Li}_3\text{PO}_4[100]/\text{vac}$	40	–	–
$\gamma\text{-Li}_3\text{PO}_4[010]/\text{vac}$	73	–	–
$\beta\text{-Li}_3\text{PO}_4[010]/\text{Li}(\tilde{\Omega}_1)$	39	1.8	Fig. 5(a)
$\gamma\text{-Li}_3\text{PO}_4[100]/\text{Li}(\tilde{\Omega}_2)$	33	1.6	–
$\gamma\text{-Li}_3\text{PO}_4[010]/\text{Li}(\tilde{\Omega}_3)$	31	0.0	Fig. 5(b)
$\gamma\text{-Li}_3\text{PS}_4[010]/\text{vac}$	20	–	–
$\gamma\text{-Li}_3\text{PS}_4[010]/\text{Li}$	–216	–0.1	Fig. 7
$\gamma\text{-Li}_3\text{PS}_4[010]/\text{Li}_2\text{S}[110]$	16	1.0	Fig. 9

focus on interfaces with the nonpolar (110) surface of Li_2O . We considered multiple interface configurations $\tilde{\Omega}$, and two representative cases are depicted in Fig. 1. In general, we found that beyond three layers, the dependence of the results on the total number of electrolyte layers was negligible, although the number of layers does affect the symmetry of the resulting slab. Depending on the Li slab symmetry, the number of electrolyte layers had to be adjusted in order to maintain symmetric interfaces within the cell, as illustrated by the geometries shown in Fig. 1.

The calculated lattice constant for Li_2O ($Fm\bar{3}m$) in our simulations was 4.53 \AA . For both of the reported configurations, the supercell geometry is an orthorhombic cell with lattice constants equal to 4.53 \AA in the [100] direction and 6.31 \AA in the [1–10] direction. The lattice constant in the [110] direction depends on the amount of metallic Li in the simulated system.

For the interface labeled $\text{Li}_2\text{O}/\text{Li}(\tilde{\Omega}_1)$, the metallic Li structure is patterned after the Li structure within Li_2O , as illustrated in Fig. 1(a). The interface labeled $\text{Li}_2\text{O}/\text{Li}(\tilde{\Omega}_2)$, shown in Fig. 1(b), is representative of several similar interfaces whose Li positions were derived from optimizing an initial configuration generated by adding approximately 1 \AA of random noise to the Li metal positions in the $\tilde{\Omega}_1$ structure. Interestingly, this randomized structure search method resulted in a structure equivalent to a strained fcc Li structure cleaved along its (110) plane. As part of our configuration search, we discovered several variations of this structure with lower symmetry and very similar energies, consistent with the complicated phase diagram of Li [39].

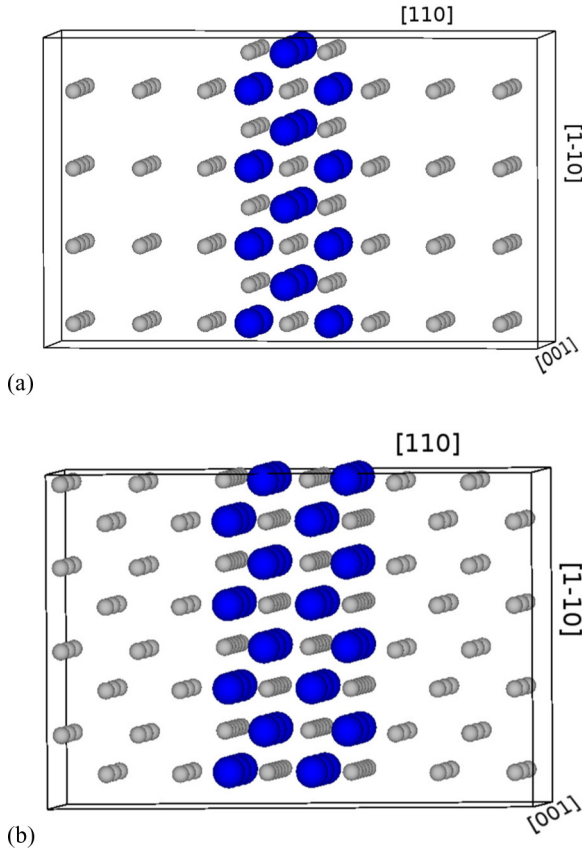


FIG. 1. (Color online) Structural diagrams of supercells for $\text{Li}_2\text{O}/\text{Li}$ interfaces with Li and O represented by small gray and larger blue balls respectively. The lattice directions refer to the Miller indices of the cubic Li_2O lattice. In both structures the Li_2O was cleaved along the (110) and an interface was formed with one of two different Li configurations. The Li structure in subfigure (a), labeled the $\text{Li}_2\text{O}/\text{Li}(\tilde{\Omega}_1)$ configuration, is an orthorhombic structure derived from the Li positions within Li_2O . The Li structure in subfigure (b), the $\text{Li}_2\text{O}/\text{Li}(\tilde{\Omega}_2)$ configuration, corresponds to a strained fcc Li structure cleaved along the (110) plane.

For both configurations, we calculated $\tilde{\gamma}_{ab}$, which varies linearly with n_b as predicted by Eq. (6) and shown in Fig. 2. The calculated values of $\tilde{\gamma}_{ab}^{\text{lim}}$ are 30 and 26 $\text{meV}/\text{\AA}^2$ for the $\text{Li}_2\text{O}/\text{Li}(\tilde{\Omega}_1)$ and the $\text{Li}_2\text{O}/\text{Li}(\tilde{\Omega}_2)$ configurations, respectively, while the associated values of σ are 6.1 and 0.2 $\text{meV}/\text{\AA}^2/\text{Li}$. The large value of $\sigma(\tilde{\Omega}_1)$ is due to the unphysical nature of the orthorhombic Li configuration. The small value of $\sigma(\tilde{\Omega}_2)$ on the other hand suggests that this configuration is close to a preferred equilibrium geometry of Li and that $\tilde{\Omega}_2 \approx \tilde{\Omega}_2$. According to the reasoning outlined in Eq. (7), this implies that for this case, the coherent limit of the interface energy is close to the physical value so that for this interface, $\tilde{\gamma}_{ab}^{\text{lim}}(\tilde{\Omega}) \approx \gamma_{ab}(\tilde{\Omega})$.

The two configurations exhibit markedly different Li structures, both within the Li slab and at the $\text{Li}_2\text{O}/\text{Li}$ interface. The similarity in their interface energies in spite of their dissimilar structures suggests that multiple interface configurations may exist near this value of the interface energy.

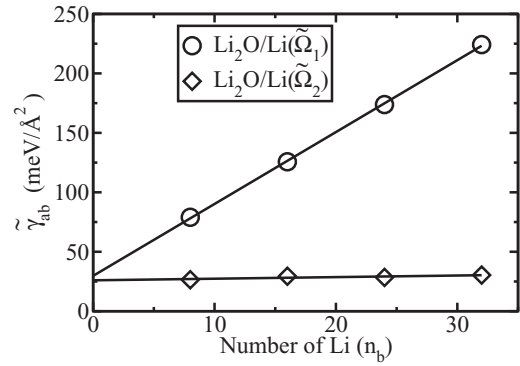


FIG. 2. Plot of $\tilde{\gamma}_{ab}$ for the $\text{Li}_2\text{O}/\text{Li}(\tilde{\Omega}_1)$ and the $\text{Li}_2\text{O}/\text{Li}(\tilde{\Omega}_2)$ interfaces showing the linear relationship described in Eq. (6). The y intercept of the graph corresponds to $\tilde{\gamma}_{ab}^{\text{lim}}$ and the slope corresponds to σ . The numerical values are summarized in Table II.

2. $\text{Li}_2\text{S}/\text{Li}$

We considered multiple possible interfaces between Li_2S and Li metal, and four representative cases are depicted in Fig. 3. The calculated lattice constant for Li_2S ($Fm\bar{3}m$) was 5.57 \AA . The supercells used to model the interfaces were orthorhombic, and in the interface plane the cell dimensions were 5.57 \AA in the $\langle 100 \rangle$ directions and 7.88 \AA in the $\langle 110 \rangle$ directions. The cell dimension orthogonal to the interface varied depending on the number of electrolyte layers and Li atoms. In each case the number of electrolyte layers was adjusted so that the interfaces on both sides of the simulation cell were symmetric.

The $\tilde{\Omega}_1$ and $\tilde{\Omega}_2$ configurations shown in Figs. 3(a) and 3(b) are comprised of Li_2S cleaved along a (110) plane combined with an orthorhombic Li structure based on the Li placements in Li_2S . As shown in Fig. 4, the extrapolated interface energy for $\text{Li}_2\text{S}/\text{Li}(\tilde{\Omega}_1)$ is $\tilde{\gamma}_{ab}^{\text{lim}} = 47 \text{ meV}/\text{\AA}^2$, while the slope of the fit line is $\sigma = 4 \text{ meV}/\text{\AA}^2/\text{Li}$. For $\text{Li}_2\text{S}/\text{Li}(\tilde{\Omega}_2)$, the interface energy is $\tilde{\gamma}_{ab}^{\text{lim}} = 11 \text{ meV}/\text{\AA}^2$, while the slope of the fit line is also $\sigma = 4 \text{ meV}/\text{\AA}^2/\text{Li}$. While both configurations are based on similar Li and Li_2S geometries, they differ in the relative alignment of the two materials at the interface. This is reflected in the similarity of $\sigma(\tilde{\Omega}_1)$ and $\sigma(\tilde{\Omega}_2)$ as well as the appreciable difference between $\tilde{\gamma}_{ab}^{\text{lim}}(\tilde{\Omega}_1)$ and $\tilde{\gamma}_{ab}^{\text{lim}}(\tilde{\Omega}_2)$.

The third configuration, $\text{Li}_2\text{S}/\text{Li}(\tilde{\Omega}_3)$, shown in Fig. 3(c) is the interface between the (110) face of Li_2S and a Li configuration generated by allowing sets of randomized initial Li positions to relax. As in the $\text{Li}_2\text{S}/\text{Li}(\tilde{\Omega}_2)$ configuration, the Li positions in the Li metal at the interface closely resemble the positions of Li atoms in Li_2S . The $\text{Li}_2\text{S}/\text{Li}(\tilde{\Omega}_3)$ configuration is not closely related to any readily identifiable Li structure but its density is comparable to the fcc and bcc phases of bulk Li. The extrapolated interface energy is $\tilde{\gamma}_{ab}^{\text{lim}} = 19 \text{ meV}/\text{\AA}^2$, and the slope of the fit line is $\sigma = 0.2 \text{ meV}/\text{\AA}^2/\text{Li}$.

The last of the four cases, shown in Fig. 3(d), represents an interface between Li_2S cleaved at a (100) face and a bulk like Li structure derived from randomized Li positions. Stoichiometric Li_2S cleaved in the [100] direction results in a polar surface. It does not have identical interfaces at both

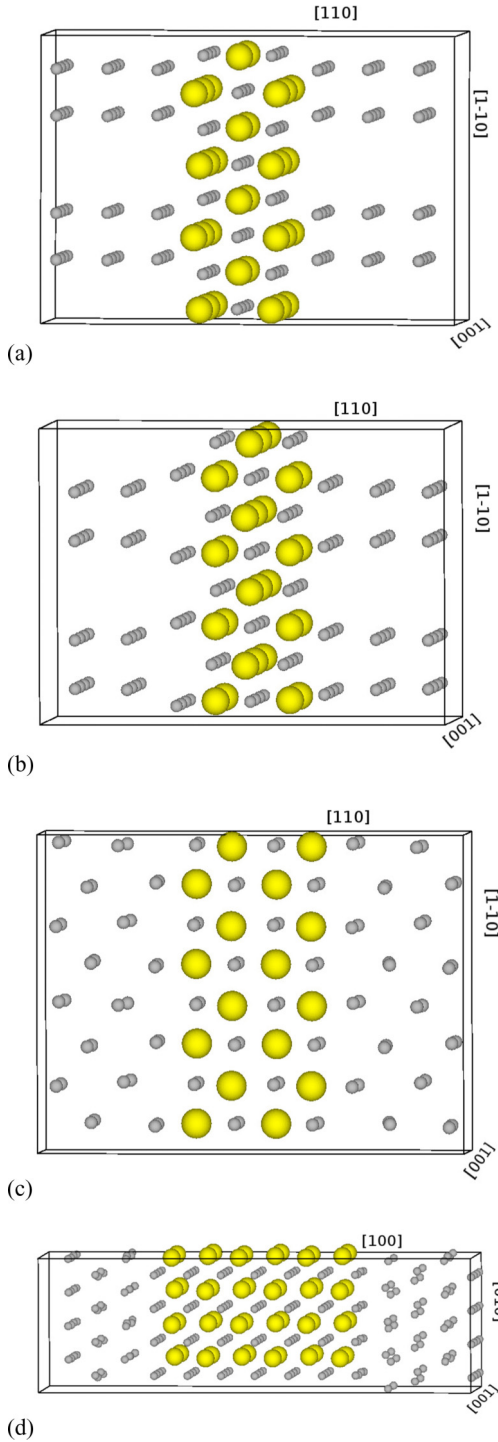


FIG. 3. (Color online) Structural diagrams of supercells for $\text{Li}_2\text{S}/\text{Li}$ interfaces with Li and S represented by small gray and larger yellow balls respectively. The lattice directions reference the Miller indices of cubic Li_2S . Four configurations are presented. (a) The $\text{Li}_2\text{S}/\text{Li}(\tilde{\Omega}_1)$ and (b) the $\text{Li}_2\text{S}/\text{Li}(\tilde{\Omega}_2)$ configurations are both based on a $[110]$ cleavage of Li_2S with the Li slab positions derived from the Li structure in Li_2S , although the interfaces have two different alignments. (c) The $\text{Li}_2\text{S}/\text{Li}(\tilde{\Omega}_3)$ has a configuration with a Li structure based on optimizing randomly generated Li positions. (d) The $\text{Li}_2\text{S}/\text{Li}(\tilde{\Omega}_4)$ configuration shows the interface between the (100) face of Li_2S and a Li structure based on optimizing randomly generated Li positions.

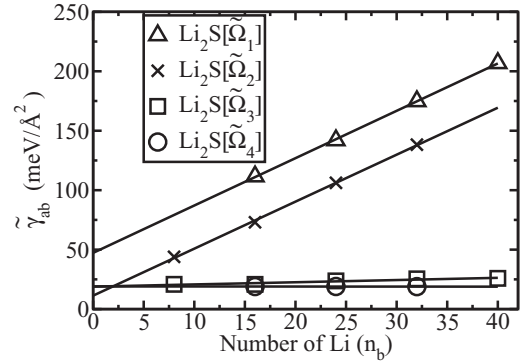


FIG. 4. Plot of $\tilde{\gamma}_{ab}$ for the $\text{Li}_2\text{S}/\text{Li}(\tilde{\Omega}_i)$ interfaces for $i = 1-4$ showing the linear relationship described in Eq. (6). The numerical values are summarized in Table II.

sides of the Li_2S slab, but is instead Li terminated on one side of the slab and S termination on the other. However, when placed in contact with Li metal, the first layer of the Li metal at the S terminated side of the slab relaxes to a configuration identical to that observed on the Li terminated side of the slab and the resulting configurations on both sides of slab are equivalent. The extrapolated interface energy for the $\text{Li}_2\text{S}/\text{Li}(\tilde{\Omega}_4)$ interface configuration is $\tilde{\gamma}_{ab}^{\text{lim}} = 19 \text{ meV}/\text{Å}^2$, and the slope of the fit line is $\sigma = 0.0 \text{ meV}/\text{Å}^2/\text{Li}$.

Interestingly, the calculated interface energy for the $\text{Li}_2\text{S}[110]$ surface and the $\text{Li}_2\text{S}[100]$ surface are very similar. This suggests that the surface energy may not depend strongly on the cleavage of the Li_2S for this system if the Li metal is not constrained. Experimental work on liquid metal/solid insulator interfaces has also observed that the interface energy does not always depend strongly on the exposed cleave of the solid [41].

3. $\text{Li}_3\text{PO}_4/\text{Li}$

We investigated the interface between metallic Li and Li_3PO_4 . Li_3PO_4 occurs in multiple phases, and we considered both the $\beta\text{-Li}_3\text{PO}_4$ ($Pmn2_1$) and the $\gamma\text{-Li}_3\text{PO}_4$ (Pnma) phases as listed in Table I. The two crystal lattices are related by a rotation, so that the $\gamma\text{-Li}_3\text{PO}_4$ **b** axis most closely resembles the $\beta\text{-Li}_3\text{PO}_4$ **a** axis, while the $\gamma\text{-Li}_3\text{PO}_4$ **a** axis resembles two times the $\beta\text{-Li}_3\text{PO}_4$ **b** axis.

Considering both phases of Li_3PO_4 , three unique surfaces were generated by flat cleavage planes parallel to the crystal lattice planes. These surfaces are the (010) surface of $\beta\text{-Li}_3\text{PO}_4$ and the (100) and (010) surfaces of $\gamma\text{-Li}_3\text{PO}_4$. We constructed Li interfaces for all three systems, and we label the resulting configurations with $\tilde{\Omega}_{1-3}$ in keeping with our previous notation. The $\beta\text{-Li}_3\text{PO}_4/\text{Li}(\tilde{\Omega}_1)$ interface between the $\beta\text{-Li}_3\text{PO}_4$ (010) surface and 36 Li atoms, as well as the $\gamma\text{-Li}_3\text{PO}_4/\text{Li}(\tilde{\Omega}_3)$ interface between the $\gamma\text{-Li}_3\text{PO}_4$ (010) surface and 48 Li atoms are both depicted in Fig. 5.

For all three configurations, we calculated $\tilde{\gamma}_{ab}$ following the methodology outlined in the formalism, and these results are shown in Fig. 6. The close similarity between the (100) plane of $\gamma\text{-Li}_3\text{PO}_4$ and the (010) plane of $\beta\text{-Li}_3\text{PO}_4$ is evident in the close agreement of the $\tilde{\gamma}_{ab}$ values for these interfaces.

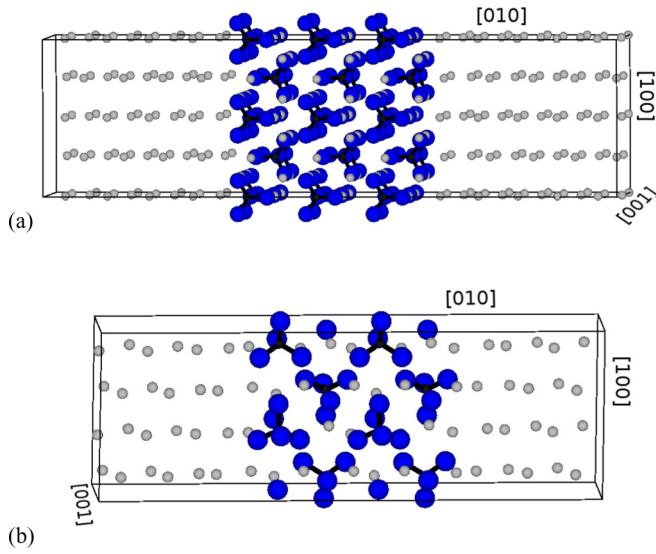


FIG. 5. (Color online) Structural diagrams of supercells for $\text{Li}_3\text{PO}_4/\text{Li}$ interfaces with Li, P, and O atoms represented by small gray, tiny black, and medium blue balls, respectively. (a) $\text{Li}_3\text{PO}_4/\text{Li}(\tilde{\Omega}_1)$ interface of [010] $\beta\text{-Li}_3\text{PO}_4$ and a Li slab. (b) $\text{Li}_3\text{PO}_4/\text{Li}(\tilde{\Omega}_3)$ interface of [010] $\gamma\text{-Li}_3\text{PO}_4$ and a Li slab.

As an additional verification of our method we also calculated the interface energy $\tilde{\gamma}_{ab}^{\text{lim}}$ for the $\beta\text{-Li}_3\text{PO}_4(\tilde{\Omega}_1)$ configuration depicted in Fig. 5(a) using a variation on the method outlined in Eq. (6). In this alternative method, the lattice constants of the orthorhombic interface cell were allowed to relax while the angles were held constant. The lattice strain energy in this method was calculated explicitly, by calculating the total energies for both the Li_3PO_4 and Li slabs in the strained configuration and comparing those energies to the corresponding values for slabs simulated using the bulk lattice constants. The interface energy estimated via this alternative method was $41 \text{ meV}/\text{\AA}^2$, in good agreement with the value of $39 \text{ meV}/\text{\AA}^2$ arrived at via the extrapolation method.

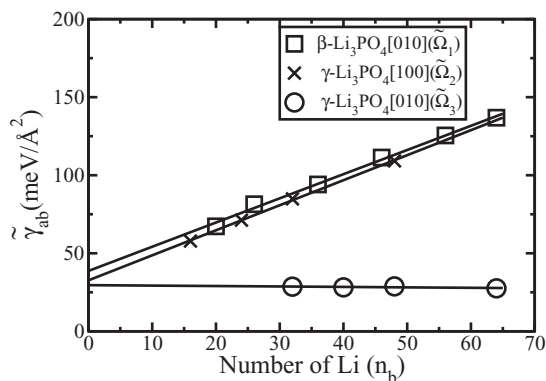


FIG. 6. Plot of $\tilde{\gamma}_{ab}$ for the $\text{Li}_3\text{PO}_4/\text{Li}(\tilde{\Omega}_i)$ interfaces for $i = 1-3$ showing the linear relationship described in Eq. (6). The numerical values are summarized in Table II.

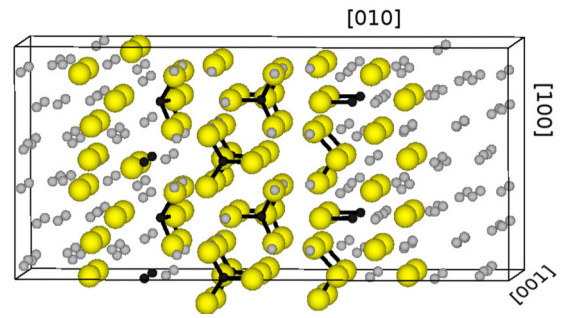


FIG. 7. (Color online) Structural diagram of $\gamma\text{-Li}_3\text{PS}_4[010]/\text{Li}$ interface with 24 Li with Li, P, and S represented by small gray, tiny black, and medium yellow balls respectively.

4. $\text{Li}_3\text{PS}_4/\text{Li}$

The interface between Li_3PS_4 and metallic Li exhibits substantial disruption of the Li_3PS_4 structure at the interface as shown in previous work [13]. While Li_3PS_4 exists in both $\beta\text{-Li}_3\text{PS}_4$ ($Pnma$) and $\gamma\text{-Li}_3\text{PS}_4$ ($Pmn2_1$) phases, the structural and energetic differences between the phases are small compared to the disruption of the electrolyte/anode surface due to Li metal. Consequently, we present quantitative results only for the $\gamma\text{-Li}_3\text{PS}_4$ (010) surface, although our results for the other phases and surfaces are similar.

This interface is visualized in Fig. 7. The PS_4 tetrahedra near the surface of Li_3PS_4 break apart and bond to the metallic Li, forming a Li_2S -like phase at the interface. This agrees well with experimental results that show the formation of a similar layer at the $\text{Li}/\text{Li}_3\text{PS}_4$ interface [42]. The disordered nature of the $\text{Li}_3\text{PS}_4/\text{Li}$ interface evident in Fig. 7 increases the variance in possible interface configurations. The interface energy calculated according to Eq. (6) was $-216 \text{ meV}/\text{\AA}^2$, as shown in Fig. 8. The large energies associated with the different chemically altered interfaces dominate the energy contributions from the lattice strain.

Observed values for $\tilde{\gamma}_{ab}$ varied between -175 and $-225 \text{ meV}/\text{\AA}^2$, with the variation due primarily to the extent of the decomposition reaction at the interface. For all of the configurations considered, the $\text{Li}_3\text{PS}_4/\text{Li}$ reaction resulted in

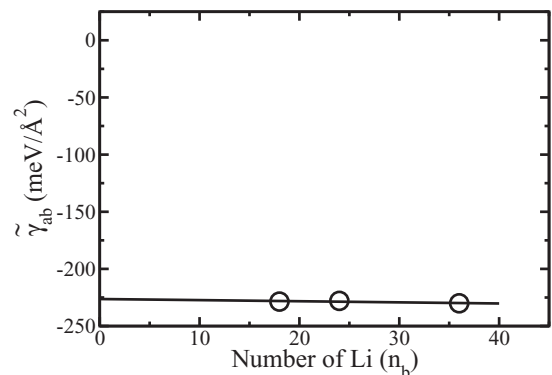


FIG. 8. Interface energy for the $\gamma\text{-Li}_3\text{PS}_4[010]/\text{Li}$ interface. The large negative value of $\tilde{\gamma}_{ab}$ is due to chemical reactions that occur at the interface. The bond breaking and bond formation at the interface dominates lattice strain effects.

the formation of a disordered Li_2S -like phase, which appeared to passivate the electrolyte against further degradation. Our zero temperature simulations are expected to underestimate the size of such a passivating layer, and it is not clear from our results alone how robust this insulating layer is. The formation of an electrically insulating layer comprised of amorphous Li_2S and Li_3P could explain the successful use of Li_3PS_4 electrolytes in experiments.

5. $\text{Li}_3\text{PS}_4/\text{Li}_2\text{S}$

Motivated by the formation of an Li_2S -like phase at the $\text{Li}_3\text{PS}_4/\text{Li}$ interface we considered the interface between the $\gamma\text{-Li}_3\text{PS}_4$ (010) and the Li_2S (110) surfaces. The Li_3PS_4 (010) face has lattice constants 6.05 and 7.55 Å, while the Li_2S (110) face has lattice constants 5.57 and 7.88 Å. The interface was constructed by aligning the dimensions appropriately and straining the Li_2S slab to the $\gamma\text{-Li}_3\text{PS}_4$ lattice. The space groups of the two materials are not compatible with the formation of identical interfaces on both sides of the simulation cell in the sandwich configuration, as can be seen in Fig. 9.

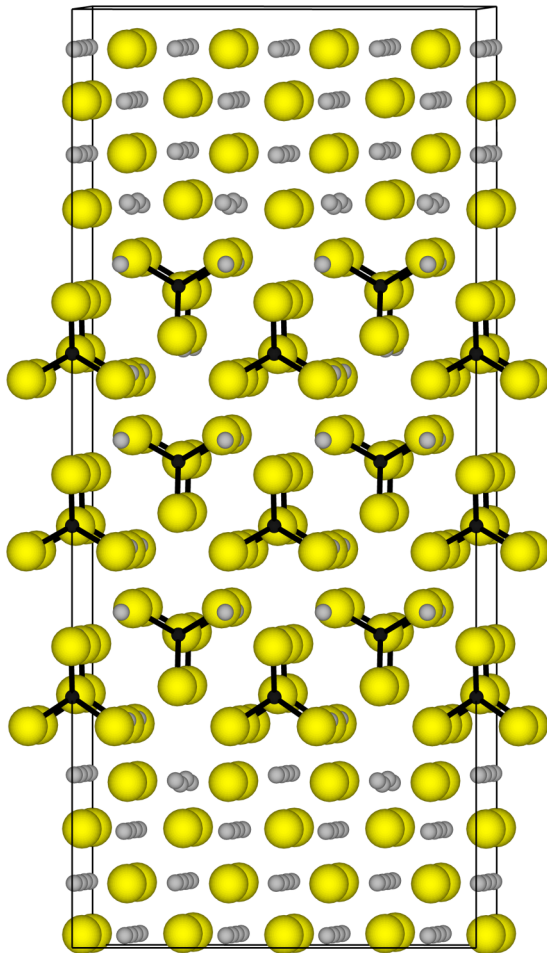


FIG. 9. (Color online) Structural diagram of $\gamma\text{-Li}_3\text{PS}_4$ [010]/ Li_2S [110] interface with Li, P, and S represented by small gray, tiny black, and medium yellow balls respectively. The asymmetry of the two interfaces is evident.

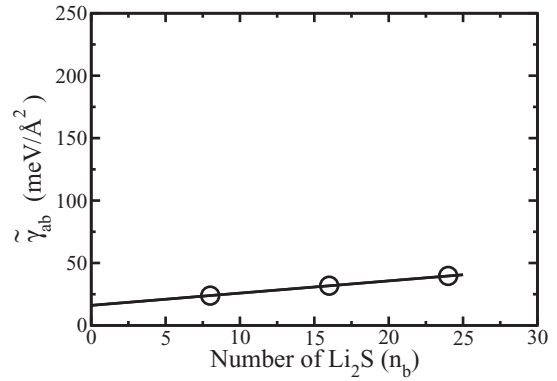


FIG. 10. Plot of $\tilde{\gamma}_{ab}$ for the $\gamma\text{-Li}_3\text{PS}_4$ [010]/ Li_2S [110] interface. Numerical values for $\tilde{\gamma}_{ab}^{\text{lim}}$ and σ are reported in Table II.

The estimated interface energy using Eq. (6) is 16 meV/Å² as shown in Fig. 10. In order to estimate the effect of the asymmetry on the interface energies, we constructed two corresponding sets of vac/ Li_3PS_4 / Li_2S /vac supercells. The interface energies in these cells were calculated using the same methodology as in the combined system, modified to account for the additional contributions of the vacuum surface energies associated with the Li_2S (110) and Li_3PS_4 (010) surfaces. We found the separate interface energies in these vacuum terminated cells to be 13 and 11 meV/Å². The average of the two separate interface energies is smaller than $\tilde{\gamma}_{ab}$ determined from the sandwich geometry because the interface geometries obtained by relaxing the vac/ Li_3PS_4 / Li_2S /vac supercells have fewer constraints. Table II lists the value obtained from the sandwich configuration, consistent with the method used for the other materials.

6. Interface energy summary

Table II summarizes the results for the calculated interface energies; selected surface energies are also included for comparison. The values for $\tilde{\gamma}_{ab}^{\text{lim}}$ and σ were determined from a linear fit to Eq. (6). The data was well represented by the linear model, even for small values of n_b , and the estimated error for the nonzero values was on the order of between 1% and 3%. The observation that the linear relationship of Eq. (6) describes the interface energies even for small values of n_b implies that the interface effects are short ranged. The notion that interface interactions are short ranged is also consistent with the observation that $\tilde{\gamma}_{ab}$ is insensitive to the magnitude of n_a .

A review of investigations of Li_2O surface energetics by Hayoun and Meyer [15] found that the reported values of the Li_2O [110] surface energy varied between 56 and 90 meV/Å². Our calculated surface energies are consistent with the literature for the nonpolar surface of Li_2O [15], Li_2S [43,44], and Li_3PO_4 [45]. For modeling the vacuum interfaces, we examined the effect of including a self-consistent dipole correction to the structural optimization of the surfaces [46]. This correction significantly decreased the size of the vacuum region needed to converge the polar Li_2O and Li_2S surfaces, but did not alter the calculated surface energies and structures. The calculated surface energy for the unreconstructed polar

surfaces are in excellent agreement with the work of Chen and Kaghazchi [43]. The calculated surface energies for the unreconstructed polar surfaces of are significantly larger than the nonpolar surface energies. This large difference in the surface energies, however, is not observed in the corresponding Li interface systems, where we find that $\tilde{\gamma}_{ab}^{\text{lim}}$ for $\text{Li}_2\text{S}[110]/\text{Li}(\tilde{\Omega}_3)$ is equal to $\tilde{\gamma}_{ab}^{\text{lim}}$ for $\text{Li}_2\text{S}[100]/\text{Li}(\tilde{\Omega}_4)$.

In general, the results of Table II show that the surface and interface energies of the materials containing oxygen are larger than the values for the corresponding sulfur-containing materials. This trend is consistent with the relatively larger formation energies for the oxide materials compared to those of the corresponding sulfides, as given in Table I.

The interface energies have been explicitly shown to be well-converged with respect to the system size in the dimension normal to the surface plane. In addition, small values of σ for some of the configurations indicate that these systems are also well converged with respect to system size in the surface plane.

In the course of this study, many interface configurations were considered; these necessarily represent only a small sample of the possible configurations. However, the relatively close agreement among the interface energies $\tilde{\gamma}_{ab}^{\text{lim}}$ for the low energy configurations reported here indicates that γ_{ab} is likely to be in this range. Within the results reported in Table II, the interface structures $\tilde{\Omega}$ with small values for both $\tilde{\gamma}_{ab}^{\text{lim}}$ and σ are likely to be more representative of the structure of physically realized interfaces.

Direct simulation of the electrolyte/Li and electrolyte/electrolyte interfaces further suggests that all of the interfaces except for that between Li_3PS_4 and metallic Li are at least metastable, while the $\text{Li}_3\text{PS}_4/\text{Li}$ interface is observed to undergo a chemical transformation. This transformation appears to produce a passivating layer with stable $\text{Li}_2\text{S}/\text{Li}$ and $\text{Li}_3\text{PS}_4/\text{Li}_2\text{S}$ interfaces. The greater magnitude of the interface energy associated with the $\text{Li}_3\text{PS}_4/\text{Li}$ interface, relative to that of the other material interfaces is due to the large energies associated with breaking and forming chemical bonds at the interface. The negative sign of the interface energy suggests that the adhesive forces at the interface exceed the cohesive forces holding the respective materials together and is probably a good indicator of a chemically active interface.

B. Analysis of partial densities of states

It is possible to gain insight into the basic interactions involved with each interface by examining the partial densities of states $[N^s(E)]$ for each system computed using Eq. (8) averaged over sets of atoms s . In order to better visualize the partial densities of states associated with Li, the $N^s(E)$ values for sets comprised of Li atoms have been multiplied by a factor 10 in all of the plots.

The interface partial densities of states are closely related to those of the corresponding bulk systems, shown in Figs. 11 and 12. The structures of the materials included in these figures are listed in Table I. For the plots of the interface and electrolyte systems, $E = 0$ is set at the top of the electrolyte valence band. The atoms were grouped into sets on the basis of the similarity of their atomic partial densities of states $N^a(E)$. For the stable interface systems, the most dramatic differences in $N^a(E)$

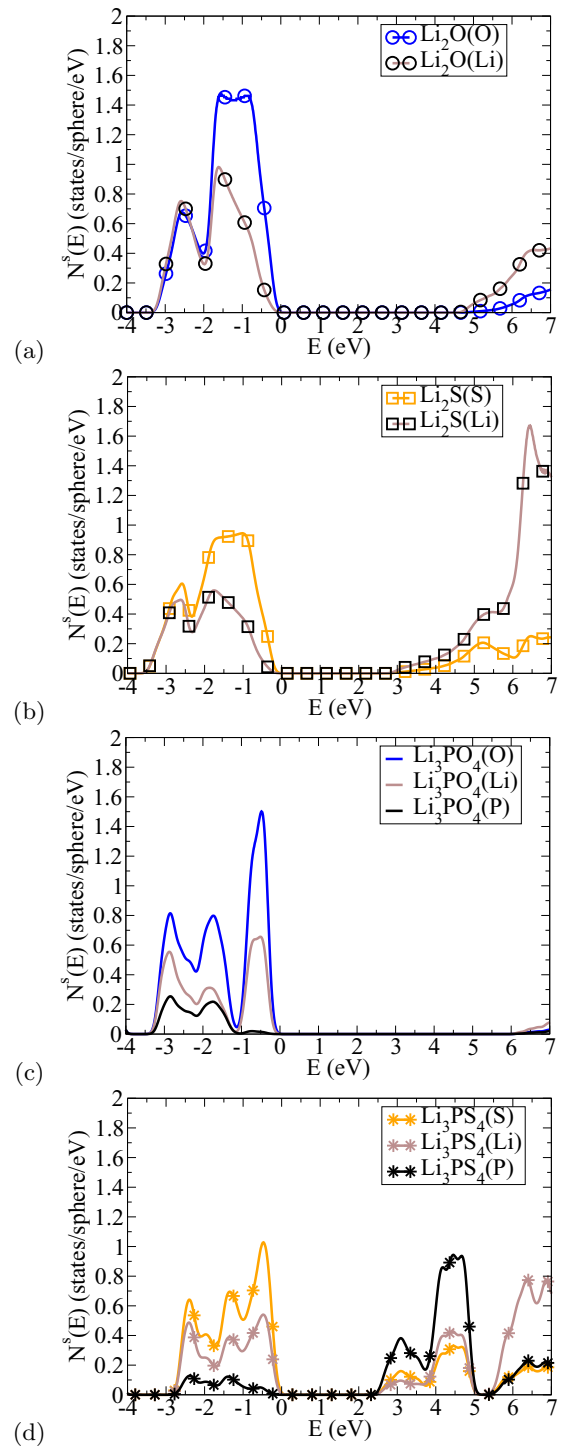


FIG. 11. (Color online) Partial densities of states for bulk (a) Li_2O , (b) Li_2S , (c) $\beta\text{-Li}_3\text{PO}_4$, and (d) $\gamma\text{-Li}_3\text{PS}_4$. In this case, the $N^s(E)$ sets are defined by the atom types, and $N^{\text{Li}}(E)$ has been scaled by a factor of 10. The energy scale is adjusted so the $E = 0$ corresponds to the top of the valence band of each material.

were those associated with the layer of Li metal atoms nearest to the interface, designated as “Li(interface)” in the legends of the plots.

The plots included here are representative of the structures and geometries discussed in Sec. III A. In particular, the $\beta\text{-Li}_3\text{PO}_4/\text{Li}$ interface is indicative of the behavior of $N^s(E)$

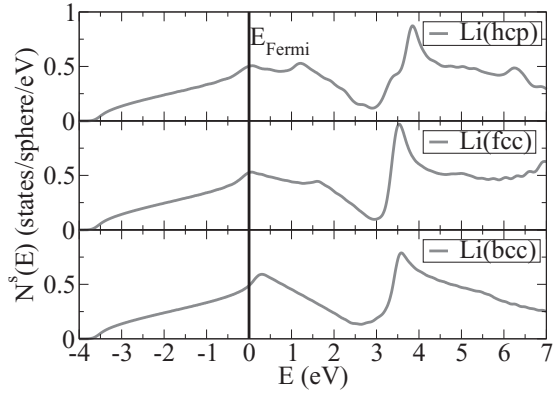


FIG. 12. $N^{\text{Li}}(E)$ scaled by a factor of 10, comparing results for the hexagonal (hcp), face centered cubic (fcc), and body centered cubic (bcc) structures.

for both the β - $\text{Li}_3\text{PO}_4/\text{Li}$ and the γ - $\text{Li}_3\text{PO}_4/\text{Li}$ interfaces. The calculated $N^s(E)$ curves are relatively insensitive to the supercell sizes.

1. $\text{Li}_2\text{O}/\text{Li}$

As shown in Fig. 13(a), for the $\text{Li}_2\text{O}/\text{Li}(\tilde{\Omega}_1)$ interface $N^s(E)$ for the Li_2O is relatively similar to the bulk density shown in Fig. 11(a). The metallic Li states on the other hand differ significantly from the bulk $N^s(E)$ given in Fig. 12. The bottom of the Li (slab) bands are near the top of the Li_2O valence bands and the Fermi level of the system is 0.8 eV higher than in the bulklike Li structure shown in Fig. 11(a). The density associated with the Li in the first layer of the metallic slab exhibit both Li_2O -like and Li slablike character in the corresponding energy ranges.

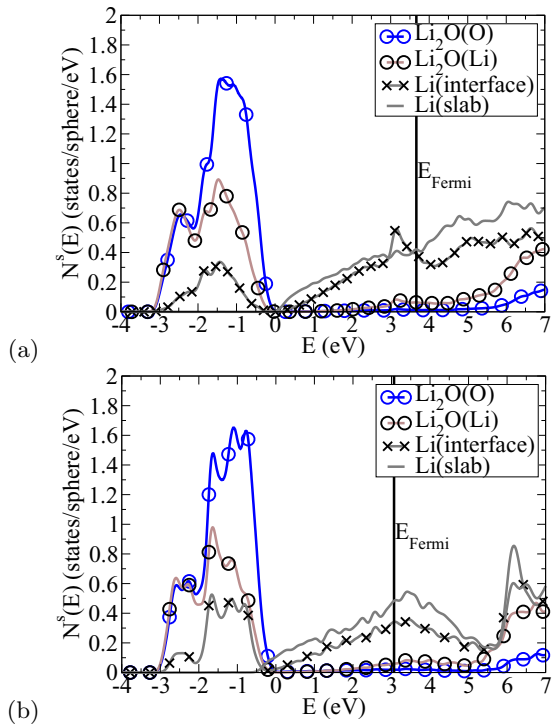


FIG. 13. (Color online) Partial densities of states for the $\text{Li}_2\text{O}/\text{Li}$ interfaces in the (a) $\tilde{\Omega}_1$ and (b) $\tilde{\Omega}_2$ configurations.

As shown in Fig. 13(b), for the $\text{Li}_2\text{O}/\text{Li}(\tilde{\Omega}_2)$ interface, the Li_2O $N^s(E)$ is also relatively unchanged from that of bulk Li_2O . Consistent with our earlier identification of the Li slab as bulk-like for this configuration, we observe that the states within the Li slab are very similar to those for bulk Li shown in Fig. 12, while $N^s(E)$ for the Li at the interface exhibits a mixture of Li_2O -like and Li-like states. The observation that the states are relatively unchanged from the bulk outside of the first layer of is in good agreement with our results from the previous section, which showed that the difference in interface energy between systems with multiple layers of Li could be attributed to lattice strain and not to interactions at the interface. For both cases, the relatively small modifications relative to the bulk density of states agrees well with the observed stability of these interfaces.

2. $\text{Li}_2\text{S}/\text{Li}$

The partial densities of states of the Li_2/Li interfaces are shown in Fig. 14. For all four of the interface configurations, the contributions from the occupied states of Li_2S are similar to those of the bulk shown in Fig. 11(b). There is some variation in the $N^s(E)$ curves in Fig. 14 due to varying degrees of undercoordination of the S atoms at the interfaces. In particular, for the $\tilde{\Omega}_1$ structure shown in Fig. 14(a), the upper peak can be attributed to the under-coordinated interface S site seen in Fig. 3(a). For configurations $\tilde{\Omega}_1$, $\tilde{\Omega}_2$, and $\tilde{\Omega}_3$, the Fermi level appears to lie within the conduction band of Li_2S . A more detailed analysis shows that these contributions are confined to the surface layer of the Li_2S slab; the bulk layers have no appreciable occupancy of the conduction band states. $N^s(E)$ for configurations $\tilde{\Omega}_1$ (a) and $\tilde{\Omega}_2$ (b) represent highly strained models of the Li slabs and the corresponding Li(slab) contributions differ significantly from that of bulk Li shown in Fig. 12. Configurations $\tilde{\Omega}_3$ (c) and $\tilde{\Omega}_4$ (d) have Li slabs that are closer to the bulk geometry and the corresponding curves are similar to that of bulk Li (apart from \mathbf{k} -point sampling errors). Interestingly, for both of these configurations, the Li (slab) contribution begins approximately -1 eV below the top of the valence band of Li_2S . It is also interesting to note that the configuration $\tilde{\Omega}_4$ formed from the polar [100] surface of Li_2S , in this sandwich geometry behaves very similarly to the configuration $\tilde{\Omega}_3$ which was formed from the non polar [110] surface.

3. $\text{Li}_3\text{PO}_4/\text{Li}$

In the partial densities of states for the β - $\text{Li}_3\text{PO}_4/\text{Li}$ interface shown in Fig. 15, the Li_3PO_4 states are even less affected by the presence of Li metal than the electrolyte states in the $\text{Li}_2\text{O}/\text{Li}$ and $\text{Li}_2\text{S}/\text{Li}$ interfaces. The top of the Li_3PO_4 valence band is below the bottom of the metallic Li band. As in the cases of Li_2O and Li_2S interfaces, there is a small amount of occupied electrolyte conduction states just at the interface.

4. $\text{Li}_3\text{PS}_4/\text{Li}$

The partial density of states for a γ - $\text{Li}_3\text{PS}_4/\text{Li}$ interface is shown in Fig. 16 with separate panels for the three main regions. The Li slab PDOS in the top panel closely resembles the $N^s(E)$ of bulk Li as shown in Fig. 12. Similarly, the $N^s(E)$ for the electrolyte region shown in the bottom panel resembles that of bulk γ - Li_3PS_4 shown in Fig. 16. The bottom of the

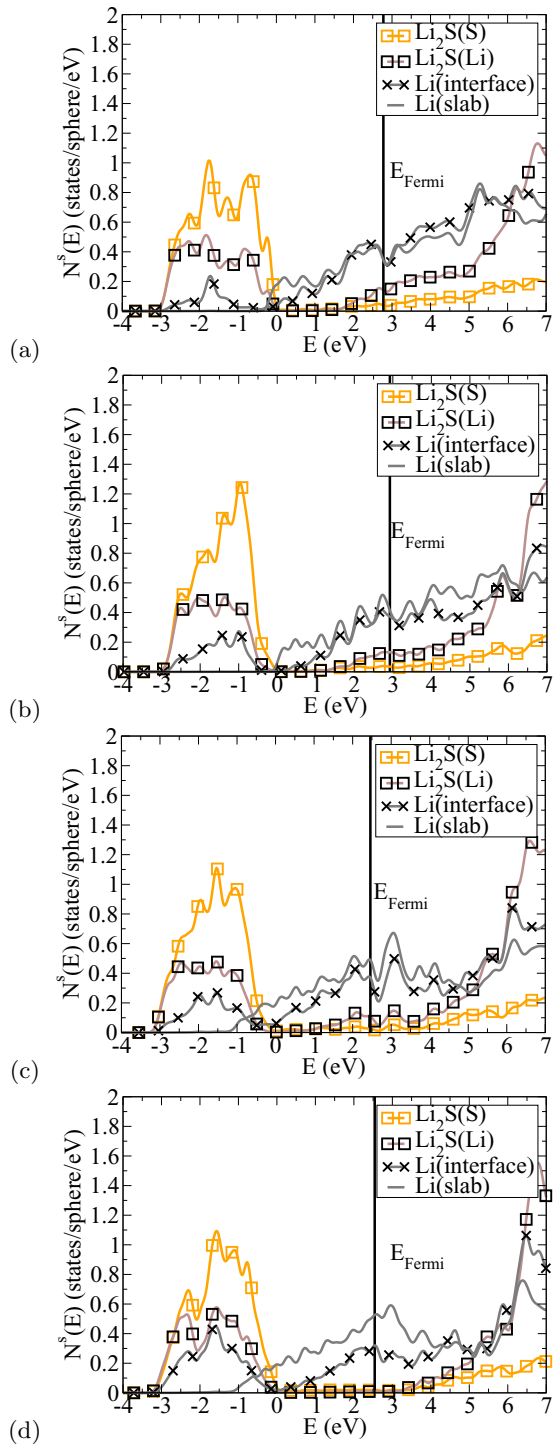


FIG. 14. (Color online) Partial densities of states for the $\text{Li}_2\text{S}/\text{Li}$ interfaces for the (a) $\tilde{\Omega}_1$, (b) $\tilde{\Omega}_2$, (c) $\tilde{\Omega}_3$, and (d) $\tilde{\Omega}_4$ configurations.

Li slab band lies 1.5 eV below the top of the valence band of the electrolyte. The Fermi level for the system, which is determined by the Li slab, lies just below the conduction band of the remaining Li_3PS_4 .

The interface $N^s(E)$ plots are given in the middle panel of Fig. 16 show the reaction products at the interface. The Li (electrolyte) set refers to Li which interact with P as evidenced by their contributions in the energy range of -7 to -8 eV corresponding to the $3s$ state of P. The Li (interface)

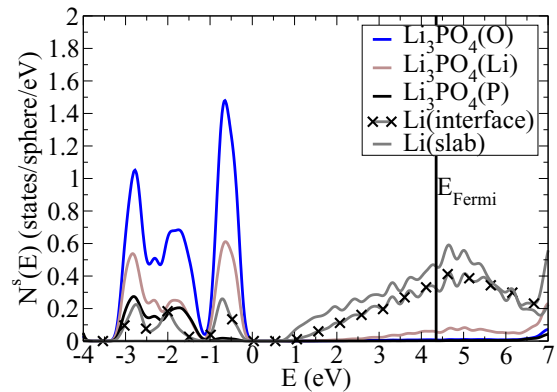


FIG. 15. (Color online) Partial density of states for $\text{Li}_3\text{PO}_4/\text{Li}$ interface in the $\tilde{\Omega}_1$ configuration.

contributions refer to the remaining Li atoms in this region and have similar qualitative behavior to the Li (interface) curves for the $\text{Li}_2\text{S}/\text{Li}$ system. The S contributions are divided into “P-S bond” and “no P-S bond” sets, based on their interaction with P, analogous to the Li division.

The close resemblance of the S (no P-S bond) curve to $N^s(E)$ for the $\text{Li}_2\text{S}(\text{S})$ set shown in Fig. 14 supports the notion that the reactive layer forms a Li_2S -like phase. Correlated with the formation of Li_2S is the reduction of the P within Li_3PS_4 , which can be seen in the shift of the unoccupied P conduction band states in the bottom panel to occupied states below the system Fermi level in the middle panel.

5. $\text{Li}_3\text{PS}_4/\text{Li}_2\text{S}$

The partial density of states plot for the $\text{Li}_3\text{PS}_4/\text{Li}_2\text{S}$ interface shown in Fig. 17 illustrates that two materials are generally not reactive and the S contributions to the occupied states of both materials largely overlap in the energy range of -3.5 – 0 eV. This superposition of the Li_2S valence band and the Li_3PS_4 valence band is also seen in the reactive region of Fig. 16.

C. Interface reactions

In addition to describing equilibrium properties of the interface, we also investigated ion transport and chemical reactions involved with the interface. One process that is of particular interest is the migration of metallic Li from the anode into the electrolyte. We studied this phenomenon in the $\text{Li}_3\text{PO}_4/\text{Li}$ system and found that if we removed a Li atom from the Li slab and placed it into a stable interstitial site in the electrolyte as visualized in Fig. 18, the associated electron remained in the slab. For this system, the fact that the metallic states are well separated from those of the electrolyte allowed us to determine that the number of electrons in the metallic bands was one greater than the number of Li atoms remaining in the slab by counting the states in each energy range.

Quantitative analysis of this effect using supercells and periodic boundary conditions is complicated by the relatively large electric fields associated with the charge separation process. The partial densities of states for the system shown in Fig. 18 are strongly affected by the electric fields E_1 and E_2 which are due to the separation between the positive

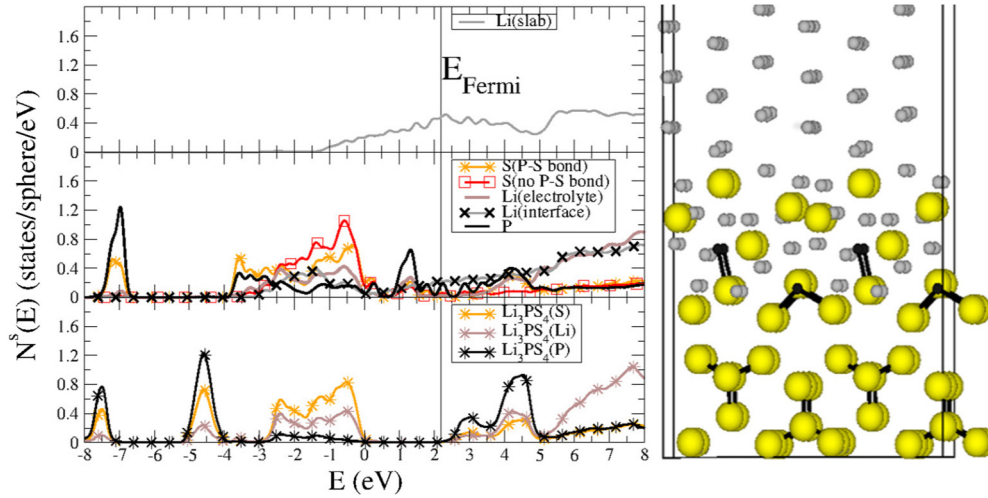


FIG. 16. (Color online) Partial density of states for γ - $\text{Li}_3\text{PS}_4/\text{Li}$ interface (left) and corresponding optimized structure (right). The three panels of the $N^s(E)$ plot correspond to the Li slab, the interface, and the electrolyte regions, respectively.

charge at the interstitial site and the excess negative charge in the metal slab. The magnitude of these electric fields can be estimated by analyzing the densities of states associated with core electrons of P at different positions within the electrolyte. We found that for this geometry, the electric fields in the interface normal direction (y) have magnitudes of approximately $eE_1 = 0.54 \text{ eV/\AA}$ and $eE_2 = 0.27 \text{ eV/\AA}$ in the regions above and below the interstitial site respectively, as indicated in Fig. 18. In order to separate the intrinsic partial densities of states of this system from the effects of these fields, we adapted the partial densities of states analysis [Eq. (8)] as follows. We assumed that the fields are well approximated as occurring only within the electrolyte and vary only in the y direction so that their effects are to shift the local band energy relative to the energy at the location (y_0) of the interstitial Li^+ so that

$$N_{\text{corr}}^s(E) = \frac{1}{M_s} \sum_{a \in s} N^a(\epsilon(E, y_a)), \quad \text{where}$$

$$\epsilon(E, y_a) = E - (y_a - y_0)eE_1\Theta(y_a - y_0) - (y_0 - y_a)eE_2\Theta(y_0 - y_a), \quad (9)$$

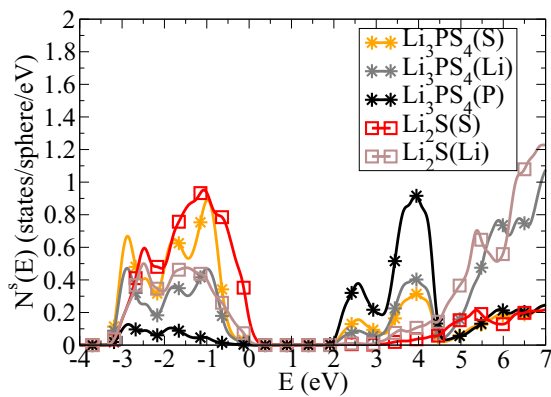


FIG. 17. (Color online) Partial density of states for the γ - $\text{Li}_3\text{PS}_4/\text{Li}_2\text{S}$ interface. The zero of energy is set to the top of the valence band of γ - Li_3PS_4

were $\Theta(x)$ denotes the Heaviside step function, eE_1 and eE_2 represent the magnitudes of the estimated electric fields mentioned above, and y_a denotes the position of atom a . The partial density of states associated with the metallic Li slab is unaffected.

$N_{\text{corr}}^s(E)$ for this system is visualized in Fig. 19 which illustrates the alignment of both the core and valence states throughout the electrolyte. While there remains some distortion of the partial densities of states curves due to the strong electric fields, the general shape and width is similar to that for the interface system without the interstitial Li^+ shown in Fig. 15, validating the electric field estimates. The interstitial Li^+ site is located only 2 \AA from one of the oxygens in Li_3PO_4 . This proximity strongly affects its partial density

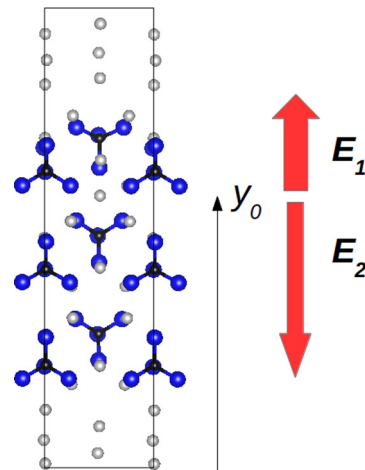


FIG. 18. (Color online) Structural diagram of a supercell of β - $\text{Li}_3\text{PO}_4[010]/\text{Li}$ with an interstitial defect and 11 Li atoms in the metallic slab. Li, P, and O sites are indicated with small gray, tiny black, and medium blue balls respectively. The vertical direction of the diagram is oriented along the interface normal direction (y). The red arrows indicate the direction, extent (length of arrow) and magnitude (width of arrow) of the electric fields E_1 and E_2 within the electrolyte.

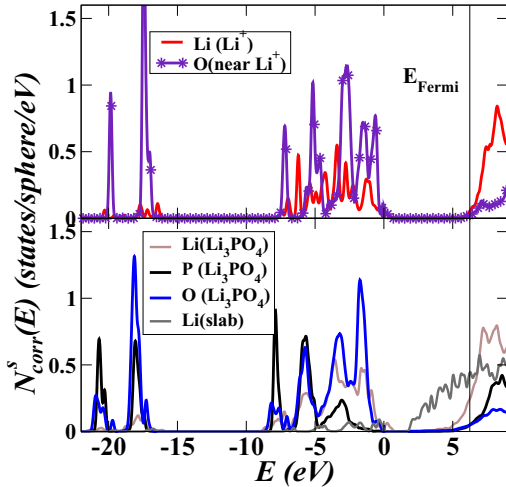
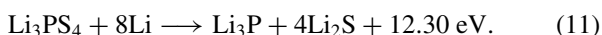
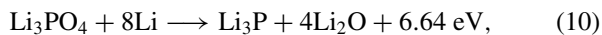


FIG. 19. (Color online) Partial density of states for β - Li_3PO_4 [010]/Li interface corresponding to the structure shown in Fig. 18 calculated according Eq. (9). The contributions for the Li interstitial (Li^+) and its nearest neighbor oxygen are plotted separately. The zero of energy is set approximately at the top of the electrolyte valence band.

of states; the corresponding $N_{\text{corr}}^s(E)$ for this unique oxygen and the interstitial Li^+ are plotted separately. $N_{\text{corr}}^s(E)$ for the interstitial Li^+ is confined to the valence energy region of the electrolyte, consistent with its characterization as an ion.

The energy associated with forming the defect configuration shown in Fig. 18 in our simulation is 2.1 eV, consistent with previous work by Santosh and co-workers [45,47]. A large component of this energy is due to the electrostatic interaction between the Li^+ and the excess negative charge in the metallic slab. The negative charge remaining in the anode is an appropriate model of a battery in an open circuit where there is no ionic or electronic current flow, consistent with the high calculated energy for Li^+ migration. By contrast, in a discharging battery, the flow of electrons in response to the chemical potential difference between the electrodes results in the anode becoming positively charged. In Li ion battery cells the anode is typically charged to +3 V or more relative to the cathode. Under these conditions we expect the transport of Li^+ ions into the electrolyte to have a substantially reduced or negligible energy barrier.

Another interesting consideration for these systems is their interface stability. In the previous section, we showed that it is possible to form stable Li_3PO_4 /Li interfaces, while the Li_3PS_4 /Li interface decomposes. In spite of this contrast, if one considers the possibility of exposing either Li_3PO_4 or Li_3PS_4 to metallic Li, both of the following reactions are exothermic according to the heats of formation calculated for the materials [13]:



In these reactions, P drastically changes its oxidation state from formally P^{+5} in Li_3PO_4 and Li_3PS_4 to P^{-3} in Li_3P . These reactions suggest that both Li_3PO_4 /Li and Li_3PS_4 /Li

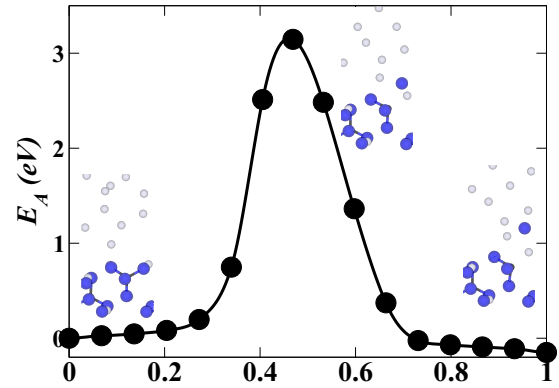


FIG. 20. (Color online) Plot of minimum energy barrier E_A (in eV) as a function of the normalized reaction coordinate for the breaking of a P-O bond at a β - Li_3PO_4 /Li interface as determined with the NEB approximation. The three inserts represent structural diagrams of the initial, maximal, and final configurations of the process using small gray, tiny black, and medium blue balls to represent Li, P, and O, respectively.

interfaces should be unstable at equilibrium. The result that Li_3PO_4 /Li interfaces are observed to be stable both computationally and experimentally [48] suggests that there is a kinetic barrier that prevents the reaction in Eq. (10) from occurring.

We considered some aspects of this activation barrier by directly breaking a P-O bond at the interface using the nudged elastic band (NEB) method to find the minimum energy barrier between two metastable O positions in the system. Because the energy of breaking the P-O bond is large compared to that of rearranging the Li atoms in the Li slab, for some of our paths, including the reported one, we imposed an artificial cost for moving the Li atoms in order to stabilize the path optimization algorithm. In general, we find that moving a O from one of the PO_4 tetrahedra in Li_3PO_4 to the Li slab, often results in a net lowering of the energy of the system, as seen in Fig. 20 and broadly consistent with Eq. (10). The NEB results for one of the many bond-breaking geometries considered are shown in Fig. 20 where the activation energy for the process is approximately 3 eV. This analysis is consistent with the existence of the kinetic barrier to the decomposition reaction 10. Apparently, for the Li_3PS_4 /Li system, no such barrier exists.

IV. DISCUSSION

One of the things we observed while constructing our interface systems was that minimizing the lattice mismatch between materials did not always result in ordered interfaces. As an example, in forming an interface between the β - Li_3PO_4 [010] surface and a bcc Li [100] surface, a supercell with three unit cells of β - Li_3PO_4 and 4 cells of bcc Li in the β - Li_3PO_4 [001] direction results in a lattice mismatch of only 5%. However, the resulting configuration has more metallic Li atoms at the interface than O atoms for them to interact with. This site mismatch is highly unfavorable and attempting to optimize such an interface dramatically alters the Li structure.

For the stable interface systems studied, the interface effects are found to be confined to within a few angstroms of the

interface, as shown by both the linearity of the calculated plots of $\tilde{\gamma}_{ab}(\tilde{\Omega}, n_b)$ versus n_b as well as the partial density of states analysis. This implies that these systems can be well modeled with relatively small supercells in the dimension normal to the interface. The small volume of the interface region suggests that, in the limit of perfect atomically sharp interfaces, the altered chemical environments at the interface may have a limited influence on the system.

We found a positive value for $\tilde{\gamma}_{ab}^{\text{lim}}(\tilde{\Omega})$ for all of the interfaces we considered except for $\text{Li}_3\text{PS}_4/\text{Li}$, which we observed to be unstable. A negative value of $\tilde{\gamma}_{ab}(\tilde{\Omega})$ implies that the bulk energies $n_a E_a + n_b E_b$ are smaller in magnitude than the total energy of the interface system $\tilde{E}_{ab}(\tilde{\Omega}, n_a, n_b)$. In other words, the interface interaction is stronger than the corresponding interactions within the bulk materials, allowing the interface to disrupt the bulk structures.

We have illustrated that interface stability is not always correctly predicted by heat of formation analysis, as shown by the stable $\text{Li}_3\text{PO}_4/\text{Li}$ interfaces, and we explored some of the kinetic barriers that stabilize that system. For unstable systems, such as $\beta\text{-Li}_3\text{PS}_4/\text{Li}$ and $\gamma\text{-Li}_3\text{PS}_4/\text{Li}$, we have shown that partial density of states analysis can be used to identify redox reactions at the interface. Specifically, we identified the occupation of conduction band states of P at the interface consistent with its expected change in oxidation state.

As noted in the recent review paper of Li and co-workers [9], solid electrolytes have great promise for high voltage batteries in part because of their wide electrochemical windows [49]. In order to avoid the reduction or oxidation of the electrolyte by the electrodes and maintain the stability of the electrode/electrolyte interface, the lowest unoccupied electrolyte band must be offset above the anode Fermi level, and the highest occupied electrolyte band must be below the cathode Fermi level. This band offset model is qualitatively supported by the stability results in our simulated interfaces.

Another interesting application of the band offset analysis is approximate estimates of the Fermi levels associated with the electrolyte/electrode interfaces. For example, we can compare our simulations of the $\gamma\text{-Li}_3\text{PO}_4/\text{Li}$ system to a recent investigation by Sumita and co-workers [11] of the $\text{LiFePO}_4/\gamma\text{-Li}_3\text{PO}_4$ system to estimate the Fermi levels associated with an idealized $\text{Li}/\gamma\text{-Li}_3\text{PO}_4/\text{LiFePO}_4$ system. While the calculational details for $\text{LiFePO}_4/\gamma\text{-Li}_3\text{PO}_4$ differed somewhat from those employed in the current work, they found the Fermi level of LiFePO_4 to be approximately 1.2 eV above the top of the $\gamma\text{-Li}_3\text{PO}_4$ valence band. In our simulations of the $\text{Li}_3\text{PO}_4/\text{Li}$ interface we found the Li Fermi level to be located 4.6 eV above the $\gamma\text{-Li}_3\text{PO}_4$ valence band. This result is not shown, but the related partial density of states plot for $\beta\text{-Li}_3\text{PO}_4/\text{Li}$ is given in Fig. 15.

Using the $\gamma\text{-Li}_3\text{PO}_4$ valence band edge as a common reference, the predicted energy difference between the Fermi levels of LiFePO_4 and Li is found to be 3.4 eV. This difference happens to be in excellent agreement with the experimentally determined open circuit voltage of this system of 3.45 eV [50]. While this analysis ignores some of the complications of the real materials and more work is needed to determine to what extent the agreement is indicative, it is nonetheless suggestive.

We also demonstrated how the modeling of transport properties at electrode/electrolyte interfaces are complicated by the separation of the ionic and electronic charge. Because the internal components of a discharging battery do not maintain charge neutrality, models that do not take this into account may estimate migration barriers relevant for the open circuit battery instead.

V. CONCLUSIONS

In this work, we outlined several aspects involved with the detailed modeling of solid-solid interfaces. A practical scheme was developed to compute an intensive measure of the interface interaction $\tilde{\gamma}_{ab}^{\text{lim}}(\tilde{\Omega})$, explicitly accounting for the effects of lattice strain. This scheme enables the quantitative comparison of disparate interface geometries on a consistent basis. By considering disparate interface geometries we attempted to estimate not only the most probable value of the interface energy, but the likely extent of its variation. For the cases we studied, smaller values of $\tilde{\gamma}_{ab}^{\text{lim}}$ corresponded to more physically probable interface configurations. The interface energy formalism, combined with analysis of the interface densities of states, allowed us to characterize possible interface structures and to determine their stability for several systems relevant to the further development of solid state batteries.

We identified multiple attributes that appear to be indicative of the chemical stability of the interface for these systems. The most novel of these attributes were the sign of $\tilde{\gamma}_{ab}^{\text{lim}}$ and the relative positions of the occupied and unoccupied bands for the interface materials.

For select optimized geometries, we also investigated charge transfer processes across the interface, and we observed both the charge dissociation associated with a Li atom migrating into an electrolyte material and the change in oxidation states associated with reactivity at the interface.

ACKNOWLEDGMENTS

This work was supported by NSF grant DMR-1105485. Computations were performed on the Wake Forest University DEAC cluster, a centrally managed resource with support provided in part by the University.

-
- [1] A. P. Sutton and R. W. Balluffi, *Interfaces in Crystalline Materials* (Clarendon Press, Oxford, 1995).
 [2] M. W. Finnis, *J. Phys.: Condens. Matter* **8**, 5811 (1996).
 [3] R. Benedek, D. N. Seidman, and C. Woodward, *J. Phys.: Condens. Matter* **14**, 2877 (2002).

- [4] J. Hartford, *Phys. Rev. B* **61**, 2221 (2000).
 [5] A. Hashibon, C. Elsasser, and M. Ruhle, *Acta Mater.* **53**, 5323 (2005).
 [6] M. Benoit, C. Langlois, N. Combe, H. Tang, and M.-J. Casanove, *Phys. Rev. B* **86**, 075460 (2012).

- [7] S. Lu, Q.-M. Hu, M. P. J. Punkkinen, B. Johansson, and L. Vitos, *Phys. Rev. B* **87**, 224104 (2013).
- [8] E. Fu, Y. Fang, M. Zhuo, S. Zheng, Z. Bi, Y. Wang, M. Tang, X. Ding, W. Han, H. Luo, J. Baldwin, A. Misra, and M. Nastasi, *Acta Mater.* **64**, 100 (2014).
- [9] J. Li, C. Ma, M. Chi, C. Liang, and N. J. Dudney, *Adv. Energy Mater.* **5**, 1401408 (2015).
- [10] M. Haruta, S. Shiraki, T. Ohsawa, T. Suzuki, A. Kumatani, Y. Takagi, R. Shimizu, and T. Hitosugi, *Solid State Ionics* (2015).
- [11] M. Sumita, Y. Tanaka, M. Ikeda, and T. Ohno, *J. Phys. Chem. C* **119**, 14 (2015).
- [12] K. Leung and A. Leenheer, *J. Phys. Chem. C* **119**, 10234 (2015).
- [13] N. D. Lepley, N. A. W. Holzwarth, and Y. A. Du, *Phys. Rev. B* **88**, 104103 (2013).
- [14] E. A. Mikajlo, K. L. Nixon, V. A. Coleman, and M. J. Ford, *J. Phys.: Condens. Matter* **14**, 3587 (2002).
- [15] M. Hayoun and M. Meyer, *Surf. Sci.* **607**, 118 (2013).
- [16] M. M. Islam and T. Bredow, *J. Phys. Chem. C* **113**, 672 (2009).
- [17] A. Lichanot, M. Gelize, C. Larrieu, and C. Pisani, *J. Phys. Chem. Solids* **52**, 1155 (1991).
- [18] W. Mackrodt, *Phys. Chem. Miner.* **15**, 228 (1988).
- [19] T. Ouazzani, A. Lichanot, and C. Pisani, *J. Phys. Chem. Solids* **56**, 915 (1995).
- [20] M. D. Radin, J. F. Rodriguez, F. Tian, and D. J. Siegel, *J. Am. Chem. Soc.* **134**, 1093 (2012).
- [21] N. Seriani, *Nanotechnol.* **20**, 445703 (2009).
- [22] A. Sutjianto, S. Tam, R. Pandey, L. Curtiss, and C. Johnson, *J. Nucl. Mater.* **219**, 250 (1995).
- [23] Z. Liu, W. Fu, E. A. Payzant, X. Yu, Z. Wu, N. J. Dudney, J. Kiggans, K. Hong, A. J. Rondinone, and C. Liang, *J. Am. Chem. Soc.* **135**, 975 (2013).
- [24] J. Haruyama, K. Sodeyama, L. Han, K. Takada, and Y. Tateyama, *Chem. Mater.* **26**, 4248 (2014).
- [25] P. Hohenberg and W. Kohn, *Phys. Rev.* **136**, B864 (1964).
- [26] W. Kohn and L. J. Sham, *Phys. Rev.* **140**, A1133 (1965).
- [27] P. E. Blöchl, *Phys. Rev. B* **50**, 17953 (1994).
- [28] P. Giannozzi, S. Baroni, N. Bonini, M. Calandra, R. Car, C. Cavazzoni, D. Ceresoli, G. L. Chiarotti, M. Cococcioni, I. Dabo, A. D. Corso, S. de Gironcoli, S. Fabris, G. Fratesi, R. Gebauer, U. Gerstmann, C. Gougoussis, A. Kokalj, M. Lazzeri, L. Martin-Samos, N. Marzari, F. Mauri, R. Mazzarello, S. Paolini, A. Pasquarello, L. Paulatto, C. Sbraccia, S. Scandolo, G. Sclauzero, A. P. Seitsonen, A. Smogunov, P. Umari, and R. M. Wentzcovitch, *J. Phys.: Condens. Matter* **21**, 395502 (2009).
- [29] N. A. W. Holzwarth, A. R. Tackett, and G. E. Matthews, *Comp. Phys. Commun.* **135**, 329 (2001).
- [30] J. P. Perdew and Y. Wang, *Phys. Rev. B* **45**, 13244 (1992).
- [31] H. J. Monkhorst and J. D. Pack, *Phys. Rev. B* **13**, 5188 (1976).
- [32] H. Jónsson, G. Mills, and K. W. Jacobsen, in *Classical and Quantum Dynamics in Condensed Phase Simulations*, edited by B. J. Berne, G. Ciccotti, and D. F. Coker (World Scientific, Singapore, 1998), pp. 385–404.
- [33] G. Henkelman, B. P. Uberuaga, and H. Jónsson, *J. Chem. Phys.* **113**, 9901 (2000).
- [34] G. Henkelman and H. Jónsson, *J. Chem. Phys.* **113**, 9978 (2000).
- [35] A. Kokalj, *J. Mol. Graphics Modell.* **17**, 176 (1999).
- [36] A. Kokalj, *Comp. Mater. Sci.* **28**, 155 (2003).
- [37] K. Momma and F. Izumi, *Appl. Crystallogr.* **44**, 1272 (2011).
- [38] D. A. Young, *Phase Diagrams of the Elements* (University of California Press, 1991).
- [39] M. Hanfland, K. Syassen, N. Christensen, and D. Novikov, *Nature (London)* **408**, 174 (2000).
- [40] Z. D. Hood, C. Kates, M. Kirkham, S. Adhikari, C. Liang, and N. A. W. Holzwarth, *Solid State Ionics* (2015).
- [41] J.-G. Li, *J. Am. Ceram. Soc.* **75**, 3118 (1992).
- [42] T. Yamada, S. Ito, R. Omoda, T. Watanabe, Y. Aihara, M. Agostini, U. Ulissi, J. Hassoun, and B. Scrosati, *J. Electrochem. Soc.* **162**, A646 (2015).
- [43] Y.-X. Chen and P. Kaghazchi, *Nanoscale* **6**, 13391 (2014).
- [44] H. Park, H. S. Koh, and D. J. Siegel, *J. Phys. Chem. C* **119**, 4675 (2015).
- [45] K. C. Santosh, R. C. Longo, K. Xiong, and K. Cho, *J. Electrochem. Soc.* **161**, F3104 (2014).
- [46] L. Bengtsson, *Phys. Rev. B* **59**, 12301 (1999).
- [47] K. C. Santosh, K. Xiong, R. C. Longo, and K. Cho, *J. Power Sources* **244**, 136 (2013).
- [48] D. Danilov, R. A. H. Niessen, and P. H. L. Notten, *J. Electrochem. Soc.* **158**, A215 (2011).
- [49] J. B. Goodenough and K.-S. Park, *J. Am. Chem. Soc.* **135**, 1167 (2013).
- [50] J. B. Goodenough and Y. Kim, *Chem. Mater.* **22**, 587 (2010).